Materials and Design 160 (2018) 601–610

Contents lists available at ScienceDirect

Materials and Design

journal homepage: www.elsevier.com/locate/matdes

Unlocking the significant role of shell material for lithium-ion battery safety

Lubing Wang [a,b], Sha Yin [a,b], Zhexun Yu [c], Yonggang Wang [d], T.X. Yu [e], Jing Zhao [f], Zhengchao Xie [f], Yangxing Li [c,*], Jun Xu [g,h,**]

[a] Department of Automotive Engineering, School of Transportation Science and Engineering, Beihang University, Beijing, 100191, China
[b] Advanced Vehicle Research Center (AVRC), Beihang University, Beijing, 100191, China
[c] Central Research Institute, Huawei Technologies Co., LTD, Longgang District, Shenzhen, 518129, China
[d] Mechanics and Materials Science Research Center, Ningbo University, Zhejiang 315211, China
[e] Department of Mechanical & Aerospace Engineering, The Hong Kong University of Science and Technology, Clear Water Bay, Kowloon, Hong Kong
[f] Department of Electromechanical Engineering, University of Macau, 999078, Macau
[g] Department of Mechanical Engineering and Engineering Science, The University of North Carolina at Charlotte, Charlotte, NC 28223, United States
[h] North Carolina Motorsports and Automotive Research Center, The University of North Carolina at Charlotte, Charlotte, NC 28223, United States

HIGHLIGHTS

- Dynamic experiments were designed and conducted for battery shell
- Mechanical behaviors were studied considering direction, strain rate and stress triaxiality index
- A strain rate dependent constitutive model with fracture criterion was established
- Finite element models were established to verify the constitutive model
- Strain rate and strength effect on short-circuit property were discussed

GRAPHICAL ABSTRACT

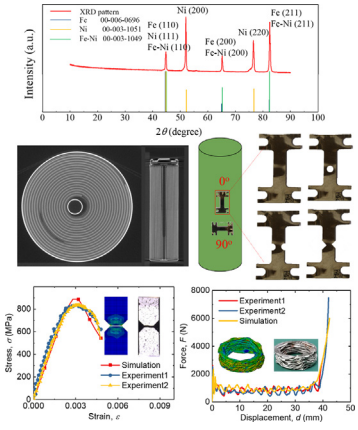

ARTICLE INFO

Article history:
Received 5 August 2018
Received in revised form 31 August 2018
Accepted 1 October 2018
Available online 2 October 2018

Keywords:
Lithium-ion battery shell
Dynamic behavior
Constitutive modeling
Strain rate dependency
Internal short-circuit

ABSTRACT

The cylindrical lithium-ion battery has been widely used in 3C, xEVs, and energy storage applications and its safety sits as one of the primary barriers in the further development of its application. Among all cell components, the battery shell plays a key role to provide the mechanical integrity of the lithium-ion battery upon external mechanical loading. In the present study, target battery shells are extracted from commercially available 18,650 NCA (Nickel Cobalt Aluminum Oxide)/graphite cells. The detailed material analysis is conducted to reveal a full understanding of the material. Then, the dynamic behavior of the battery shell material is experimentally investigated. Both theoretical constitutive and numerical models have been developed, capable to describe mechanical behaviors of the battery shell material upon impact loading. It is the first time to discover that the strain rate effect of the shell material shall be considered for the mechanical integrity of the battery and high strength of the shell material may contribute to an early short-circuit triggering. The quantitative relationship is also established between

* Corresponding author.
** Correspondence to: J. Xu, Department of Mechanical Engineering and Engineering Science, The University of North Carolina at Charlotte, Charlotte, NC 28223, United States.
E-mail address: jun.xu@uncc.edu (J. Xu).

https://doi.org/10.1016/j.matdes.2018.10.002

short-circuit and material strength. Results lay a solid foundation towards providing a theoretical safety design guidance for the shell material choice of cylindrical lithium-ion batteries.

1. Introduction

The cylindrical lithium-ion battery has been widely used in 3C, xEVs, and energy storage applications, as the first-generation commercial lithium-ion cells. Among three types of lithium-ion cell format, the cylindrical continue to offer many advantages compared to the prismatic and pouch cells, such as quality consistency and cost. As such, the most commercially successful EVs—Tesla is using thousands of cylindrical lithium-ion cells to power the car, from traditional 18,650 to current 21,700 size.

Safety is the key and fundamental performance of the battery. Due to inevitable abusive scenarios such as overcharging [1,2], penetration [3,4], overheating [5–7] and high-speed collision [7,8], various types of failure behaviors of battery component materials, thermal runaway or even fire/explosion may occur to power lithium-ion batteries (LIBs), posing great threatens to the society [9–12]. Calorimeter technology is usually used to investigate the thermal and burning behaviors of lithium-ion battery; the burning LIB could ignite adjacent batteries in the battery pack and cause the entire pack into fire or explosion consequences [13]. Doughty et al. shared their views on the safety of lithium-ion battery and discussed the typical failure modes [14]. Mechanical integrity of LIBs now becomes a determinant factor for electric vehicle safety, and it attracts global attentions from both industry and academy, however, limited progress has been achieved due to its complexity nature. Generally, battery shells serve as the protective layer for LIBs to withstand external mechanical loading and sustain the integrity of electrochemical functioning environment. Understanding the mechanical behaviors of LIB shell material especially dynamic behaviors shall play

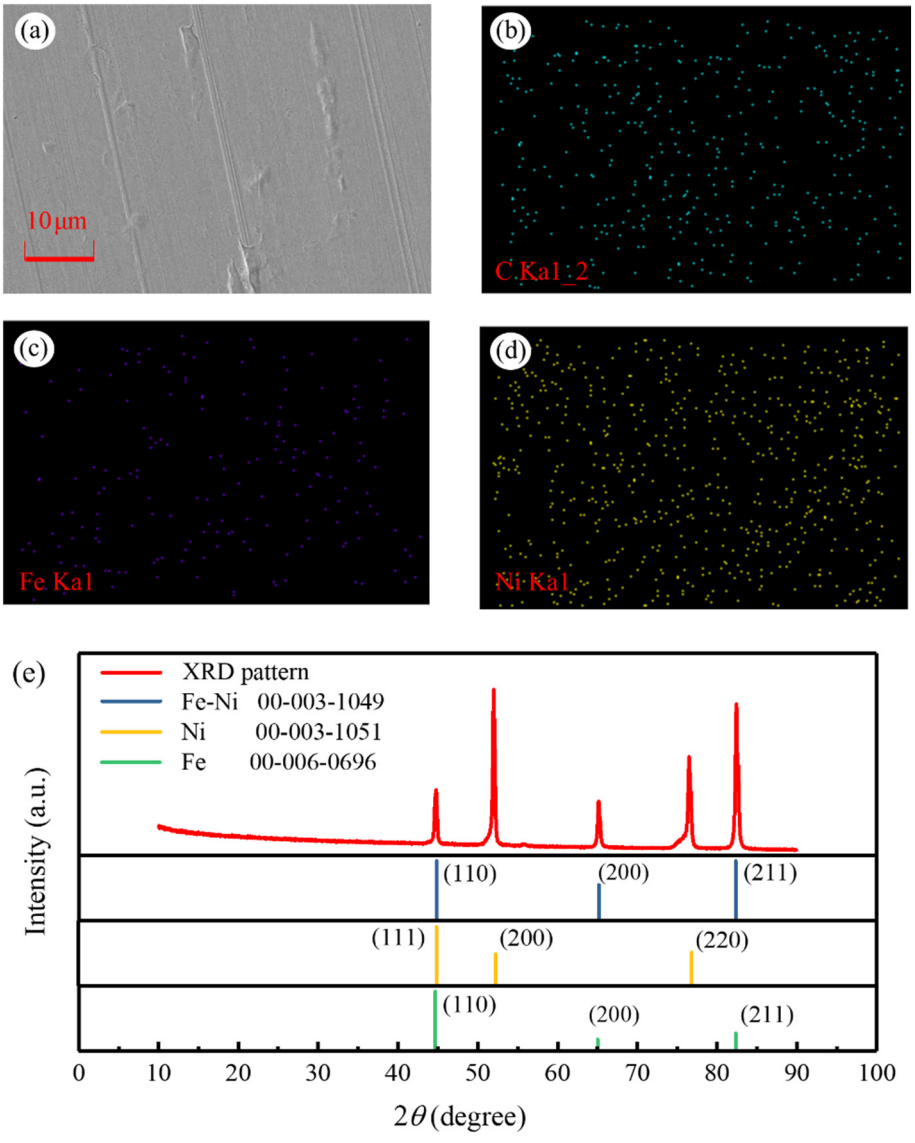

Fig. 1. Material analysis of the 18,650 battery shell: (a) SEM image of the shell surface; (b), (c), (d) element mapping of the shell; (e) XRD pattern of the shell.

a paramount role in unraveling the mechanical integrity of the LIB cell and pack.

Historically, mechanical studies of lithium-ion battery components were more focused on inner components [15–19] and the related interfaces behaviors [20,21]. Zhang et al. [22] presented experimental and numerical studies on the constitutive behavior and evolution of failure in LIB electrodes. Xu et al. [23] studied the coupled effects of strain rate and solvent on separators' dynamic mechanical behaviors. As for battery shell material, some researchers committed to improve the strength and corrosion resistance of the battery shell through the addition of Ce [24] and CeLa [25]. So far, the only publication reporting on the mechanical properties of Lithium-ion battery shell available was authored by Zhang et al. [26] on cylindrical battery shell. They conducted part of the tests to determine plastic and fracture properties from sub-sized specimens cut from lateral part of the cans and built the Modified Mohr-Coulomb (MMC) fracture model to predict crack initiation and propagation of shell casing. Their results showed that the model can predict the failure characteristics under quasi-static loading. Obviously, their model does not include the dynamic behavior of the material which is a governing loading factor in real-world impact loading scenarios. More recently, Kisters et al. [8] conducted the impact tests on lithium-ion cells and detected that the critical force changed significantly over different loading speeds. Further, a computational model of 18,650 lithium-ion battery developed by considering the strain rate (dynamic effect) of jellyroll itself was established, and the results were validated by the experiments [27].

To illuminate the dominate influence of dynamic behavior of the shell material over the safety of battery cell, this paper aims to provide a comprehensive understanding of the dynamic mechanical behaviors of LIB shell. Target shell material samples were manufactured from battery cells. Material analysis, i.e., SEM (scanning electron microscope), XRD (X-ray diffraction), and dynamic mechanical behavior characterization were conducted. A constitutive model with strain rate effect and failure model were proposed. Then, finite element models were established and further validated by experiments. The strain rate and material strength effects on short-circuit triggering time were discussed.

2. Method

2.1. Experiment setup

2.1.1. Material analysis

Cold-rolled steel are commonly used as battery shell in cylindrical lithium-ion battery and can be classified into six categories based on mechanical properties shown in Fig. S1. Target LIB shells were extracted from commercially available 18,650 NCA (Nickel Cobalt Aluminum Oxide)/graphite cylindrical lithium-ion battery with CT images shown in Fig. S2a with charge/discharge characteristic curves shown in Fig. S2b. Note that the shells are SOC (State of Charge) independent indicated by our previous study [23]. Thus, for safety reasons, the shells were obtained from batteries with SOC = 0. Here, cycling effect is not considered, for the maximum strain of the battery shell during cycling is 0.35% [28] which is in elastic stage and is recoverable, i.e., cycling of the battery does not affect mechanical performance of battery shell. All the tests were conducted at the room temperature since batteries usually work at 30–40 °C during electric vehicle operations.

SEM images of battery shell on the surface and cross-section were observed by ZEISS sigma500 to analyze its microstructure. Ion thinning technology is used to prepare the samples from cross-sectional view through Gatan Precision Ion Polishing System II 695. Material characterization was analyzed by XRD with Bruker D8 ADVANCE.

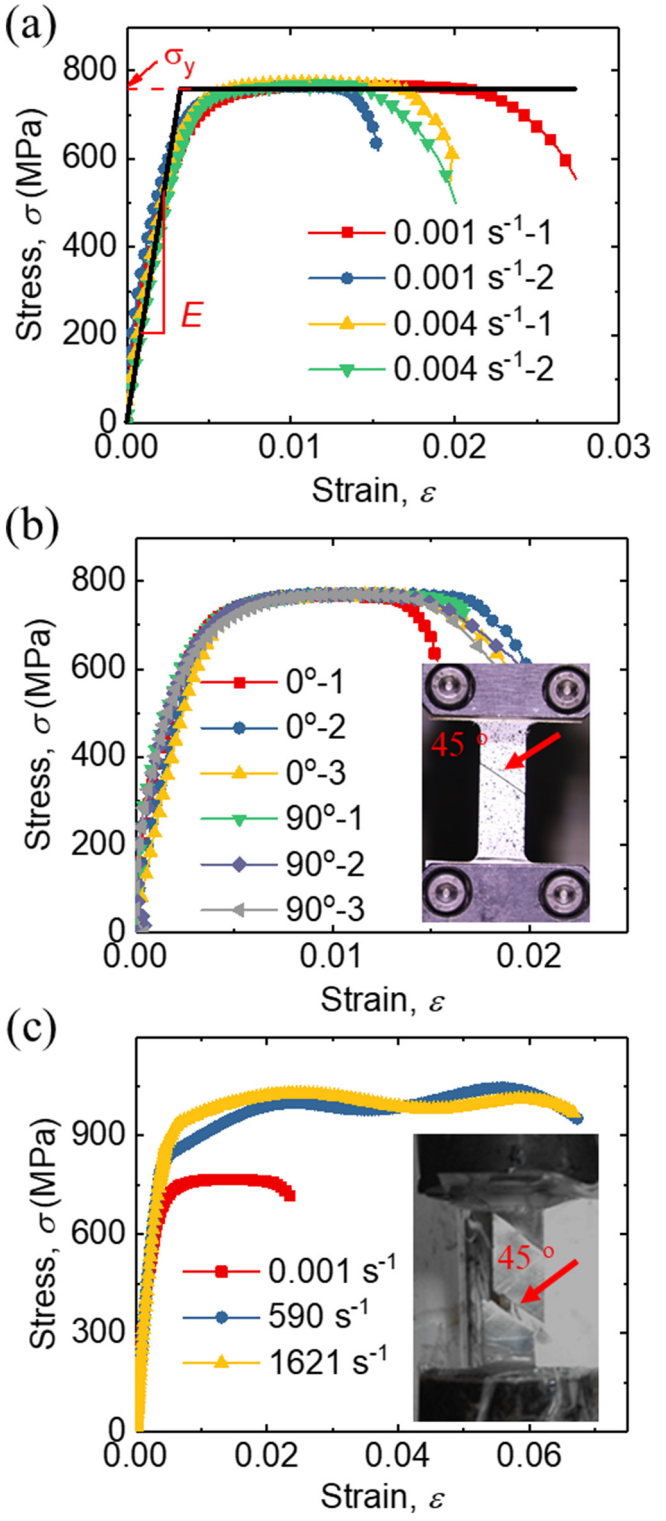

Fig. 2. Stress-strain curves of different strain rates along material directions of 0 or 90°: (a) 0.001 s^{-1} and 0.004 s^{-1} along 0°, (b) 0.001 s^{-1} along 0 and 90°, and (c) different strain rates along 0°.

2.1.2. Mechanical behavior characterization

The dog-bone shaped specimens were fabricated with 0/90° in material direction (Fig. S2c) for tensile tests. Different notched samples as O-notched, R-notched, and V-notched (Fig. S2d) were designed and manufactured for establishing failure model. Quasi-static

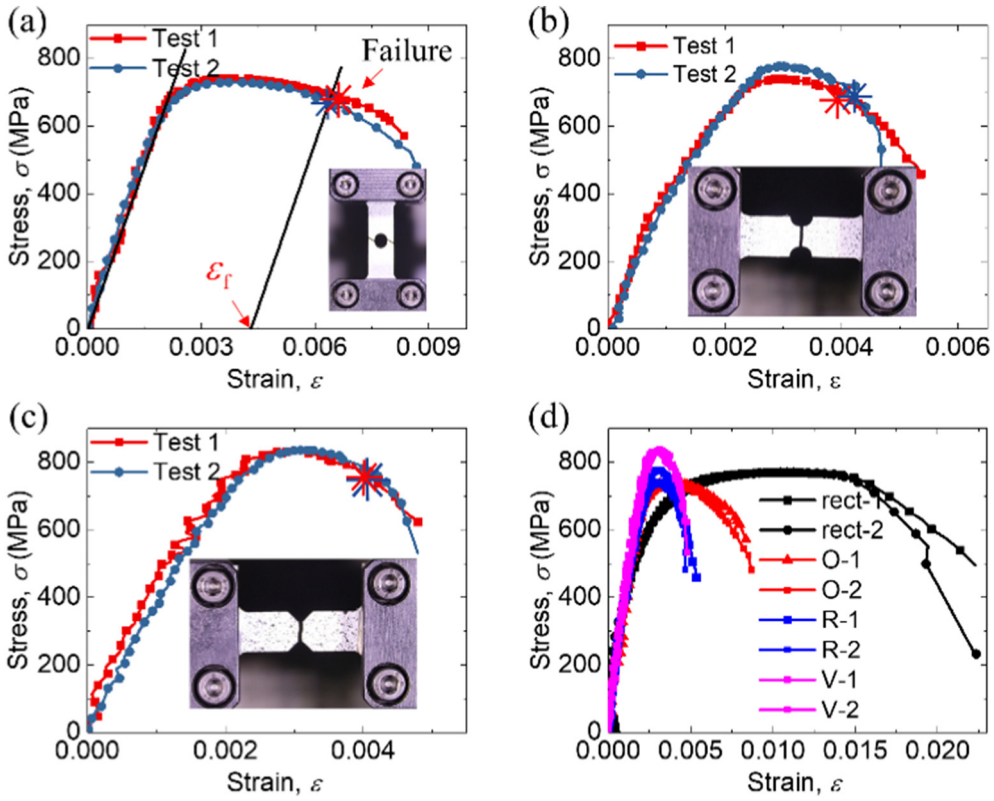

Fig. 3. Stress-strain curves of different notched samples: (a) O-notched, (b) R-notched and (c) V-notched; (d) the stress strain curves with different samples.

tensile tests were carried out by IPBF-2000 in-situ biaxial fatigue test system with XTDIC device used for non-contact 3D measurement of surface morphology, displacement, and strain (Fig. S3a). Split Hopkinson tensile bar (SHTB) technology (Fig. S3b) was adopted to investigate the dynamic behavior of battery shells. The specific description of SHTB is shown in Supplementary Note 1.

Thin-walled cylindrical structures of battery shell were designed as samples in radial indentation and axial compression experiments. For quasi-static loading, the experiments were conducted at loading speed of 5 mm/min on Instron 8801 (Fig. S4a). For dynamic loading, the samples under axial compression were conducted on servo-hydraulic testing machine HTM 5020 (Fig. S4b). Each testing scenario was repeated at least twice to ensure the repeatability of the testing data.

2.2. Theoretical models

Johnson-Cook (JC) model is generally used to describe the stress-strain behavior of the metallic materials [29,30], and results are usually satisfactory. Considering the fact that most of the material contents of LIB shell are Fe and Ni, in this case, JC model was chosen as the baseline stress-strain equation to build a constitutive relation expression for LIB shell. In JC model, the yield stress is expressed as a function of equivalent plastic strain ε_p and the natural logarithmic of the dimensionless equivalent plastic strain rate $\dot{\bar{\varepsilon}}^*$ [31,32].

$$\dot{\bar{\varepsilon}}^* = \frac{\dot{\varepsilon}}{\dot{\varepsilon}_0} \tag{1}$$

where $\dot{\varepsilon}$ is the current equivalent plastic strain rate and $\dot{\varepsilon}_0$ is a fixed reference value of it. According to the above illustration, the JC model can express the von Mises stress as a function of ε_p and $\dot{\bar{\varepsilon}}^*$, i.e.,

$$\sigma = A + B\varepsilon_p{}^n\left(1 + C\ln\dot{\bar{\varepsilon}}^*\right) \tag{2}$$

where A, B, n, Cneed to be calibrated through experiments: σ is the stress; A is the yield stress; B and n represent the effect of strain hardening; C is a material constant determined by the specific material, representing the strain rate dependence of the material.

The failure model indicates that the failure strain is sensitive to stress triaxiality index, temperature, strain rate and strain path, it can be expressed as [33].

$$\varepsilon_f = D_1 + D_2\varepsilon^{D_3\eta} \tag{3}$$

where ε_f is the plastic failure strain, and D_1, D_2, D_3 are material parameters determined by experimental data. Stress triaxiality index η is the ratio of the von Mises stress σ_m over the corresponding hydrostatic pressure σ_e.

3. Results

3.1. Experimental results

3.1.1. Material observation and analysis

Surface morphology (Fig. 1a) and element mapping (Fig. 1b–d) show that shell is composed of Fe, C, and Ni. XRD pattern illustrates that the material phase of the battery shell is mainly Fe, Ni and Fe-Ni alloy (Fig. 1e). The surface of the steel shell has been coated with a thin layer of nickel (Ni) to improve the corrosion resistance, which is

Table 1
The plastic failure strain with the stress traxiality η.

η	0.33	0.38	0.46	0.51
ε_f	0.0153	0.0043	0.0015	0.0011

also demonstrated by cross-sectional image observation (Fig. S5a). Nickel plating can be achieved through barrel plating, pre-plating and pre-plating plus barrel plating (Fig. S5b–d). The barrel plating has the advantages of high flexibility and low cost. However, due to the uneven distribution of the current density, the control of coating thickness is not as even as in theory. Instead, pre-plating method can easily control the thickness of the coating layer, and is able to achieve good uniformity, but may cause the damage or peeling off of the coating layer in the subsequent stamping and stretching process, weakening the corrosion resistance. Most of battery providers employ pre-nickel-plated steel with high mechanical strength as the shell material for cylindrical batteries.

3.1.2. Mechanical characterization

Typical stress-strain curves of battery shell along 0° under quasi-static loading show an excellent repeatability (Fig. 2a). When the strain is small, the stress increases linearly with the strain, thus the slope of the curve is defined as the Young's modulus E and calculated as $E =$ 211 GPa. With the increase of the strain, the curves exhibit plasticity and the yield stress σ_y is defined as the intersection point of the two straight lines, i.e., the linear fitting of the elastic and the plastic segments shown in Fig. 2a.

Samples along 0° and 90° under quasi-static loading were studied, results show the nickel-plated cold-rolled steel is isotropic (Fig. 2b). Strain rate effect is underpinned by the comparison between quasi-static and dynamic test results (Fig. 2c). For dynamic test, the balance of the forces applied on the two sides of the sample on SHTB equipment was verified (Supplementary Note 2). As strain rate increases, the stress-strain curves exhibit "strain hardening" phenomenon, leading to greater strength until failure. Both the dynamic and quasi-static loading share the same diagonal shear failure morphology.

Specimens with different shapes of notches may experience different stress statuses which have great influence on their failure strain ε_f. Stress triaxiality index η is used to describe the stress status, and by means of the simulation, the η value of samples with no notch, O-notched, R-notched, and V-notched could be straightforwardly calculated in Fig. S6a–d, respectively. Then, notched samples were tested under the strain rate of 0.001 s^{-1} in Fig. 3a–c. Here, ε_f is defined as the strain which corresponds to the point at which the stress decreases by 10% (Fig. 3a). ε_f decreases with the stress triaxiality index (Fig. 3d), while the exact values are summarized in Table 1. Note that samples with different shapes all exhibit a liner elastic region and share the same modulus while σ_y is increasing with the η value. The failure mode of O-notched is shear failure while those of R-notched and V-notched are tensile failures.

3.2. Modeling results

With experimental data obtained from quasi-static tests, the constitutive relation is expressed as

$$\sigma = \left(740 + 249\varepsilon_p{}^{0.46}\right) \tag{4}$$

This equation can well predict the relations in both elastic and plastic regions except the yield stress (Fig. 4a). this constitutive is no longer suitable, so the deviation increases in this region. By considering the strain rate effect with data obtained from SHTB tests, the equation can be further extended as

$$\sigma = \left(740 + 249\varepsilon^{0.46}\right)\left(1 + 0.02\ \ln\left(\frac{\dot{\varepsilon}}{\dot{\varepsilon}_0}\right)\right) \tag{5}$$

Strain rate effect can also be well captured by the model (Fig. 4b). As for the failure equation, the plastic failure strain agrees well with test

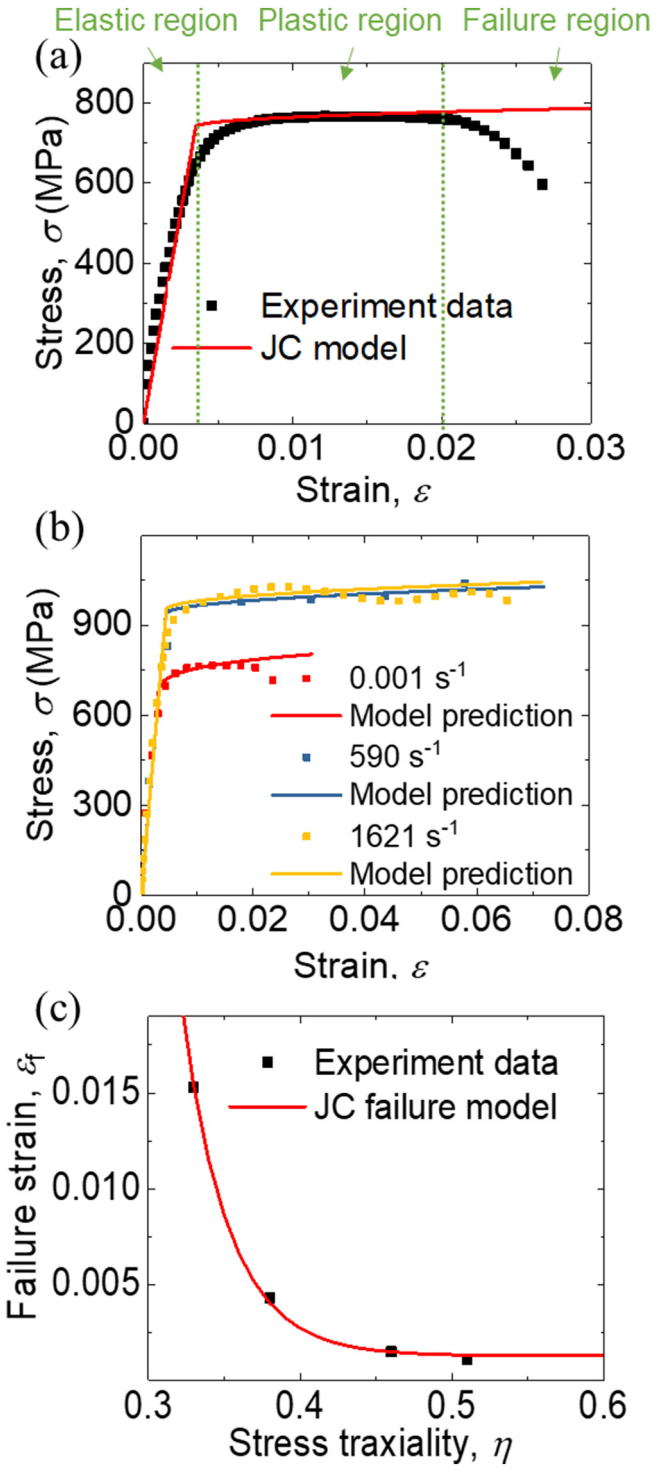

Fig. 4. Model prediction results of (a) Johnson-Cook model under quasi-static loading, (d) Johnson-Cook model under different strain rates, and (c) Johnson-Cook failure model.

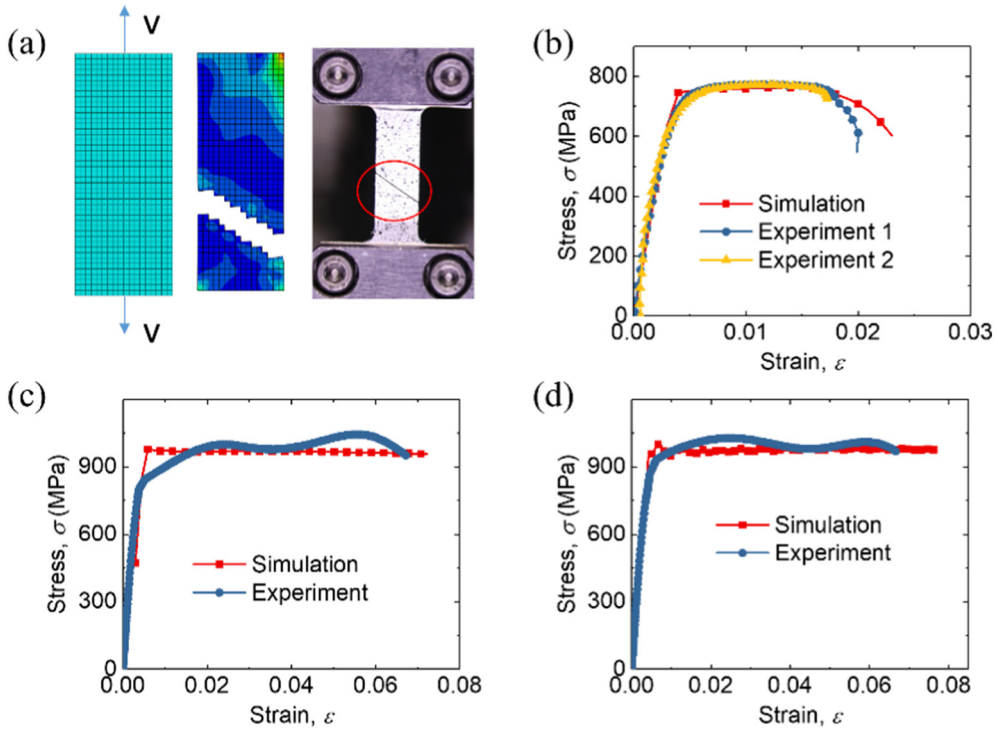

Fig. 5. (a) Illustration of FE model and the failure morphology. Comparison of simulation results and experimental results with different experimental conditions: (b) square samples with 0.001 s^{-1}, (c) square samples with 590 s^{-1}, (d) square samples with 1621 s^{-1}.

data (Fig. 4c), by the following expression:

$$\varepsilon_f = 0.001281 + 658.6e^{-32.59\eta} \tag{6}$$

3.3. Model validation

3.3.1. Validation from material perspective

The finite element models are built based on ABAQUS platform to verify the above-established constitutive model and facilitate further numerical simulation. For tensile test, the sample meshed into shell elements with 0.4 mm mesh size and 0.11 mm thickness is simplified to be in square shape with the same boundary condition setups in tests. One may clearly observe a very similar diagonal shear failure in the simulation results as that in tests (Fig. 5a). The computed stress-strain behaviors for quasi-static loading agree well with the experiment results (Fig. 5b) and it is safely to conclude that the simulation results for dynamic loading can well capture the critical properties such as the strength as well as the trend of the curves in Fig. 5c–d, the strength error is 1.7% and 2.2% at the strain rate of 590 and 1621 s^{-1}, respectively. Likewise, the established failure model is also validated through numerical simulation (Fig. 6a–c) for O-notched, R-notched and V-notched, respectively. The stress-strain curves as well as the fracture morphologies both exhibit great agreements with the experiments.

3.3.2. Validation from structure perspective

Two typical loading scenarios, i.e., indentation and compression are used to give a comprehensive validation. The corresponding finite element model setups under indentation are depicted in Fig. 7a where the indenter and the support plate are both set as the rigid bodies with general contact condition applied. Comparison between experiment and simulation results shows a good agreement (Fig. 7b). The deformation profile and ridging morphology of the samples after loading were similar in experiment and simulation along all directions (Fig. 7c). For compression tests, the FE model describing loading setups are also exact the same as in tests (Fig. 8a), and satisfactory buckling configuration results (Fig. 8b). Note that the buckling configuration here can be regarded as a typical non-symmetric collapse mode since the diameter-thick ratio $D_1/t_0 = 164 > 100$ [34]. Accordingly, the average plateau force P_m can be predicted by following equation [35]:

$$\frac{P_m}{M_0} = 22.27\left(\frac{2R_1}{t_0}\right)^{0.5} + 5.632 \tag{7}$$

while $M_0 = (2\sigma_y/\sqrt{3})(t_0{}^2/4)$, σ_y is the yield stress. Thus, the theoretical value of P_m can be calculated as 760 N, only 1.4% deviance of the experimental value.

4. Discussion

4.1. Strain rate effect

Strain rate sensitivity parameter C (in Johnson-cook model) value of two widely used engineering materials, i.e., mild steel and aluminum alloy are 0.0156 [36] and 0.0012 [37], respectively. On the other hand, C = 0.02 in nickel-plated cold-rolled steel, indicating a more severe strain rate effect. Therefore, it is imperative to focus on the strain rate effect on its shell structure as well as its role in the whole battery cell.

4.1.1. Strain rate effect on shell material

By embedding Eqs. (5) and (6) into the computational model, the strain rate effect brought by nickel-plated cold-rolled steel on the

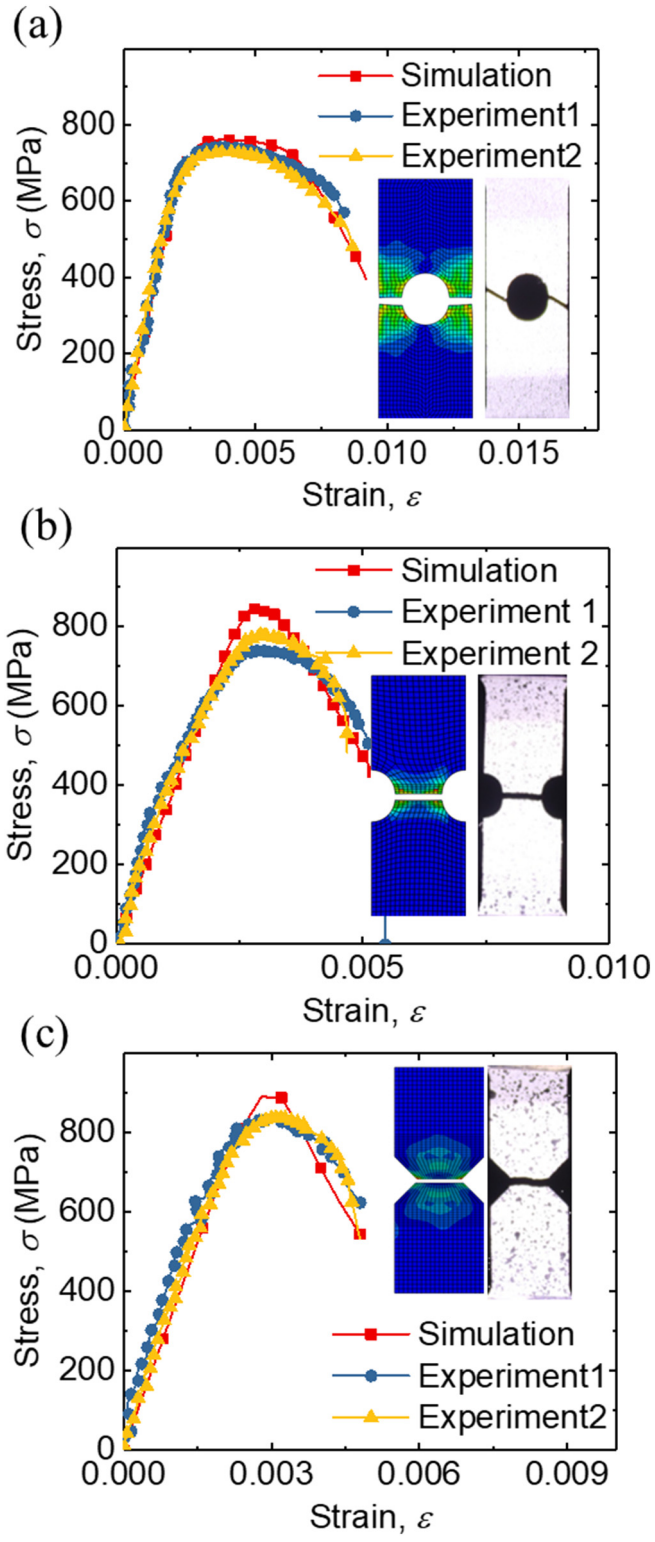

Fig. 6. The comparison of simulation results and experimental results with different experimental conditions: (a) O-notched samples with 0.001 s^{-1}, (b) R-notched samples with 0.001 s^{-1}, and (c) V-notched samples with 0.001 s^{-1}.

mechanical behavior of battery shell can be discussed. Simulation under 5 m/s loading speed show that strain rate effect can be well captured and difference between simulations using constitutive model with/without strain rate can be great, especially in terms of P_1 (peak force) and P_m (Fig. 9a). When the compression displacement becomes larger than 30 mm, the curves without strain rate exhibit significantly lower to the experimental curve. Further, illustrated by a case with 50 m/s loading speed, curves with strain rate present higher P_m (Fig. 9b). Inertia effect of the shell structure, namely, the plateau force increases with loading speed can be witness (Fig. 9c). Also, strain rate effect of shell material, i.e. the plateau force increment is more obvious with higher loading speed.

4.1.2. Strain rate effect on whole battery cell

To further underpin the importance of strain rate effect on the short-circuit behavior of batteries, here, the whole battery cell, i.e. battery shell with jellyroll is considered. The properties of jellyroll is obtained from Ref. [27] while the short-circuit criterion is adopted from Ref. [38]. The strain rate effect of nickel-plated cold-rolled steel has little influences on battery mechanical property under indentation (Fig. 10a). Interestingly, if the dynamic effect of nickel-plated cold-rolled steel is not considered in the model, a late short-circuit triggering time will be expected thus leading to the underestimation of the battery safety upon mechanical abusive loading (Table 2). Therefore, the strain rate of the nickel-plated cold-rolled steel serves as a significate factor on the battery safety.

4.2. Material strength effect

To elucidate the strength effect on battery safety, shells with different strength values (keeping all the rest of mechanical properties same) are simulated. According to the characteristics of the JC model, yield stress σ_y is changed to represent different strength values of shell materials. Result directly shows that higher strength will cause earlier short-circuit (Fig. 10b). Then, a quantitative relationship between strength and short-circuit is established as follow:

$$\varepsilon_s = \frac{d_s}{D} = -547\left(\frac{\sigma_y}{E}\right)^2 - 0.74\left(\frac{\sigma_y}{E}\right) + 0.138 \tag{8}$$

Here, ε_s is the relative short-circuit strain, D is the diameter of the battery shell, i.e., 18 mm in our case. $\sigma_y/E = \varepsilon_y$ is defined as yield strain. The prediction results shown in Fig. 10c can capture the trend of curve, and the correlation coefficient R^2 is calculated as 0.92 also indicates the satisfactory results. Cases without strain rate also share the same trend, but d_s value will be larger that further verifies the importance of strain rate effect. Traditionally, high strength is the priority concern to select battery shell material; however, it is discovered that short-circuit is easier to trigger covered by shell with higher strength. Thus, for battery safety reason, it is not always wise to choose high strength material as shell.

Nowadays, commercially available material for 18,650 battery shell usually made of low-carbon cold-rolled steel and stainless steel with various strength values (Table 3). Considering the fact that LIB is prone to be short-circuited, shell material with lower strength is recommend to select such as material #1 and #2. It is indicated that the high strength materials are not suitable for all batteries, and the selection of the shell material should be matched with the safety of the battery.

5. Conclusions

LIB shell serves as the protective layer to sustain the external mechanical loading and provide an intact electrochemical reaction environment for battery charging/discharging. Our rationale was to identify the significant role of the dynamic mechanical property of battery shell material for the battery safety.

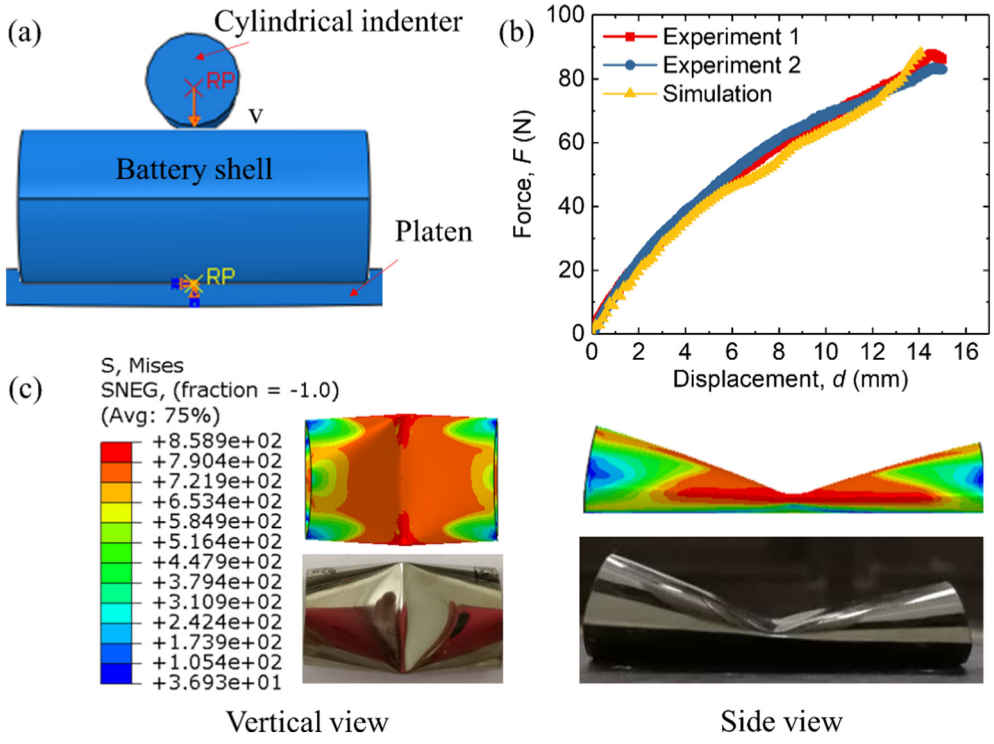

Fig. 7. The illustrations of (a) the FE model of indentation, (b) the force-displacement curves obtained from experiment and simulation, (c) the deformed configuration of samples in both experiment and simulation.

- It was observed and analyzed that current shell material is nickel-plated cold-rolled steel and its mechanical behaviors with the full consideration of material direction, strain rate effect and stress triaxiality index were experimentally investigated.
- Further, a strain rate dependent constitutive model with fracture criterion was established, and FE models were developed to validate the constitutive and failure models. Theoretical models were validated through both material and structure (as a cylindrical cell) experiments.
- The strain rate effect based on the axial compression of the shell and the entire battery was discussed, the necessity of incorporating strain rate effect into the material model was demonstrated, providing an accurate description of the battery behavior upon dynamic loading.
- High strength is one of the main targets of battery shell material, however, short-circuit is easier to be triggered when shell with higher strength upon mechanical loading. The choice of nickel plated steel on its strength is critical.

This study provides a solid dynamic constitutive modeling methodology for the LIB shell and the strain rate sensitive which may stimulate further study towards the safety design and evaluation of battery cells and packs.

Acknowledgements

This work is financially supported by, National Key Research and Development Program of China (2017YFB0103703), Opening project of State Key Laboratory of Explosion Science and Technology (Beijing Institute of Technology) with project number of KFJJ17-13M and Huawei Innovative Project.

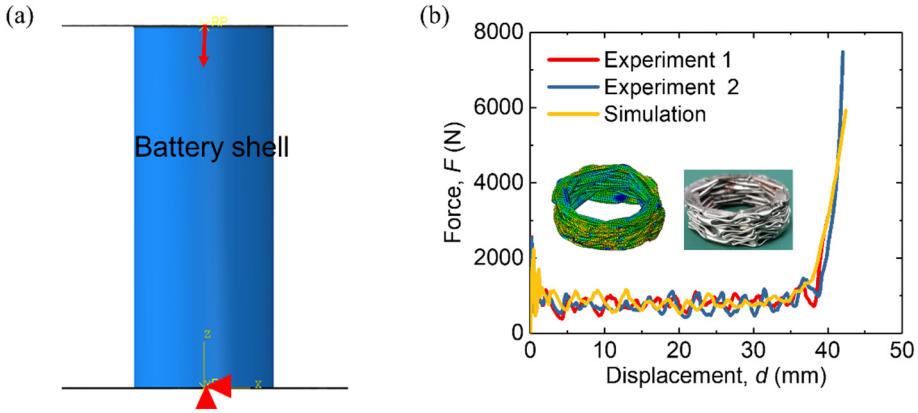

Fig. 8. Illustrations of (a) the FE model of axial compression test, (b) the results of experiments and simulations under quasi-static loading.

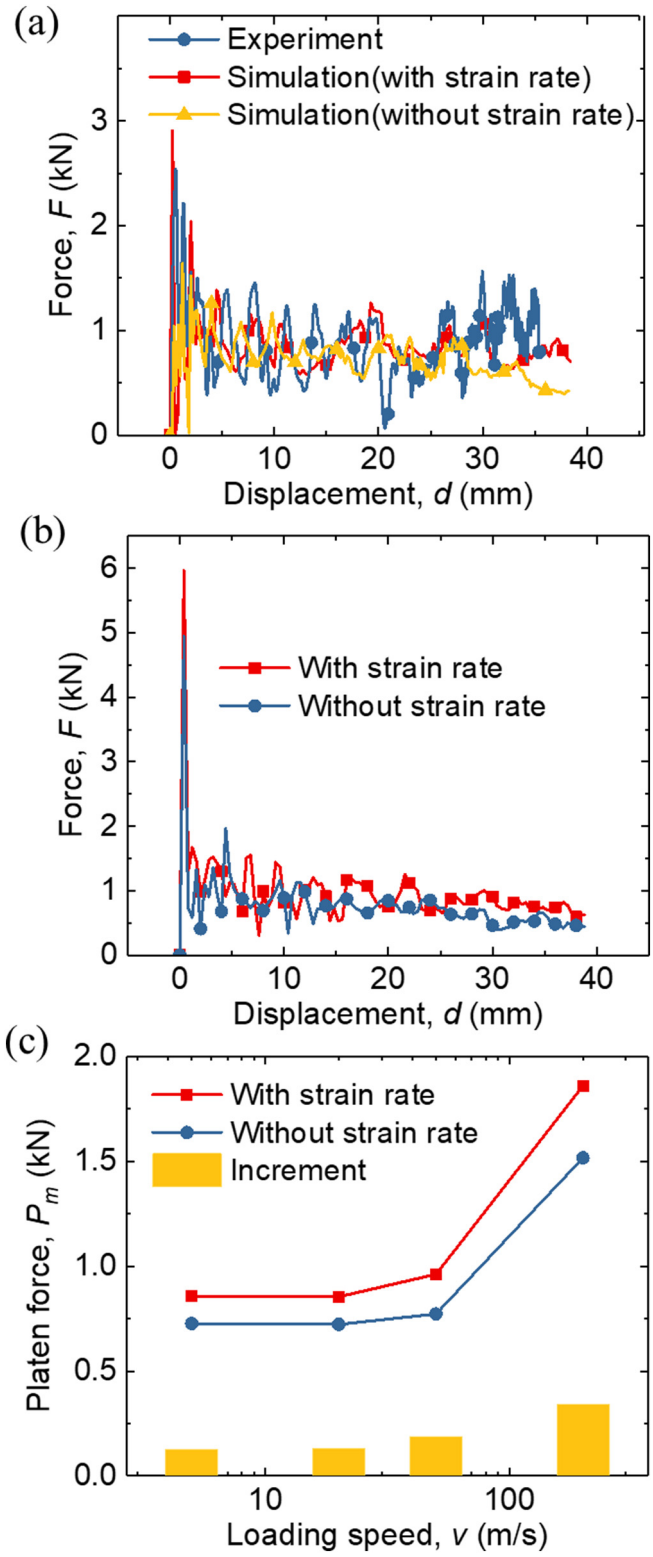

Fig. 9. Comparison between experiments and simulations: (a) the force-displacement curves under 5 m/s loading speed, (b) the force-displacement curves under 50 m/s loading speed, (c) the plateau force (increment) vs. loading speed curves under various loading speed.

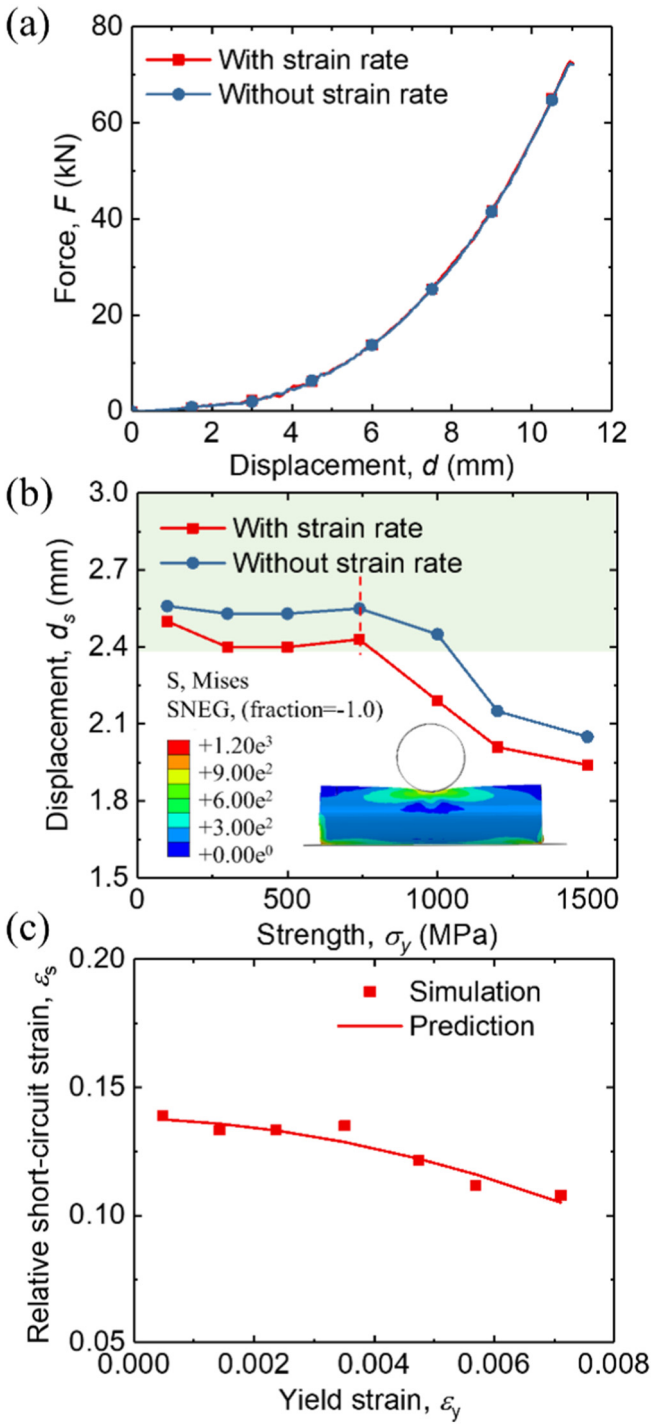

Fig. 10. Comparison between cases with strain rate or not under indentation. (a) mechanical properties at the speed of 5 m/s; (b) short-circuit triggering displacement with different strength values of material; (c) Prediction results between yield strain and short-circuit.

Conflicts of interest

There are no conflicts to declare.

Author contribution

JX and YL conceived the idea and established the major research framework. LW, YW, and ZY conducted the experiment. LW, SY, and JX carried out the theoretical analysis. All authors have participated to discuss the data and the manuscript. LW, TY, JX, and YL wrote and reviewed the manuscript.

Table 2
Short-circuit displacement of radial indentation under different loading speeds.

Loading speed v		3 m/s	5 m/s	10 m/s
Short-circuit triggering displacement d_s	Cases with strain rate	2.85 mm	1.82 mm	1.09 mm
	Cases without strain rate	2.91 mm	1.85 mm	1.11 mm

Table 3
Materials and its properties of battery shell.

Material	Lithium-ion battery	Elastic modulus (GPa)	Yield stress (MPa)	Strength (MPa)
1	HP 602030 NCA [35]	207	350	600–700
2	Panasonic 18,650 LCO [26]	160	450	500–550
3	Panasonic 18,650 LCO [36]	200	450–500	500–550
4	Panasonic 18,650 NCA	211	740	750–800

Appendix A. Supplementary data

Supplementary data to this article can be found online at https://doi.org/10.1016/j.matdes.2018.10.002.

References

[1] Q.F. Yuan, F.G. Zhao, W.D. Wang, Y.M. Zhao, Z.Y. Liang, D.L. Yan, Overcharge failure investigation of lithium-ion batteries, Electrochim. Acta 178 (2015) 682–688.
[2] Y. Zeng, K. Wu, D. Wang, Z. Wang, L. Chen, Overcharge investigation of lithium-ion polymer batteries, J. Power Sources 160 (2006) 1302–1307.
[3] Y. Xia, T. Wierzbicki, E. Sahraei, X.W. Zhang, Damage of cells and battery packs due to ground impact, J. Power Sources 267 (2014) 78–97.
[4] K.C. Chiu, C.H. Lin, S.F. Yeh, Y.H. Lin, K.C. Chen, An electrochemical modeling of lithium-ion battery nail penetration, J. Power Sources 251 (2014) 254–263.
[5] D.P. Finegan, M. Scheel, J.B. Robinson, B. Tjaden, I. Hunt, T.J. Mason, et al., In-operando high-speed tomography of lithium-ion batteries during thermal runaway, Nat. Commun. 6 (2015) 10.
[6] P. Ribière, S. Grugeon, M. Morcrette, S. Boyanov, S. Laruelle, G. Marlair, Investigation on the fire-induced hazards of Li-ion battery cells by fire calorimetry, Energy Environ. Sci. 5 (2012) 5271–5280.
[7] Z. Chen, Y. Qin, Y. Ren, W. Lu, C. Orendorff, E.P. Roth, et al., Multi-scale study of thermal stability of lithiated graphite, Energy Environ. Sci. 4 (2011) 4023–4030.
[8] T. Kisters, E. Sahraei, T. Wierzbicki, Dynamic impact tests on lithium-ion cells, Int. J. Impact Eng. 108 (2017) 205–216.
[9] Q.S. Wang, P. Ping, X.J. Zhao, G.Q. Chu, J.H. Sun, C.H. Chen, Thermal runaway caused fire and explosion of lithium ion battery, J. Power Sources 208 (2012) 210–224.
[10] A. Hammami, N. Raymond, M. Armand, Lithium-ion batteries: runaway risk of forming toxic compounds, Nature 424 (2003) 635.
[11] K. Liu, W. Liu, Y. Qiu, B. Kong, Y. Sun, Z. Chen, et al., Electrospun core-shell microfiber separator with thermal-triggered flame-retardant properties for lithium-ion batteries, Sci. Adv. 3 (2017), e1601978. .
[12] M.R. Palacín, G.A. De, Why do batteries fail? Science 351 (2016) 1253292.
[13] Y. Fu, S. Lu, K. Li, C. Liu, X. Cheng, H. Zhang, An experimental study on burning behaviors of 18650 lithium ion batteries using a cone calorimeter, J. Power Sources 273 (2015) 216–222.
[14] D. Doughty, E.P. Roth, A general discussion of Li Ion battery safety, Electrochem. Soc. Interface 21 (2012) 37–44.
[15] A. Sheidaei, X.R. Xiao, X.S. Huang, J. Hitt, Mechanical behavior of a battery separator in electrolyte solutions, J. Power Sources 196 (2011) 8728–8734.
[16] R. Clément, J. Billaud, R. Armstrong, G. Singh, T. Rojo, P.G. Bruce, et al., Structurally stable Mg-doped P2-Na2/3Mn1-yMgyO2 sodium-ion battery cathodes with high rate performance: insights from electrochemical, NMR and diffraction studies, Energy Environ. Sci. 9 (2016) 3240–3251.
[17] M. Ebner, F. Marone, M. Stampanoni, V. Wood, Visualization and quantification of electrochemical and mechanical degradation in Li ion batteries, Science 342 (2013) 716.
[18] G. Jeong, Y.U. Kim, H. Kim, Y.J. Kim, H.J. Sohn, Prospective materials and applications for Li secondary batteries, Energy Environ. Sci. 4 (2011) 1986–2002.
[19] B. Scrosati, J. Hassoun, Y.K. Sun, Lithium-ion batteries. A look into the future, Energy Environ. Sci. 4 (2011) 3287–3295.
[20] X. Yu, A. Manthiram, Electrode-electrolyte interfaces in lithium-based batteries, Energy Environ. Sci. 11 (2018) 527–543.
[21] B. Wu, S. Wang, W. Evans, Z.D. Deng, J. Yang, J. Xiao, Interfacial behaviours between lithium ion conductors and electrode materials in various battery systems, J. Mater. Chem. A 4 (2016).
[22] C. Zhang, J. Xu, L. Cao, Z. Wu, S. Santhanagopalan, Constitutive behavior and progressive mechanical failure of electrodes in lithium-ion batteries, J. Power Sources 357 (2017) 126–137.
[23] J. Xu, B. Liu, D. Hu, State of charge dependent mechanical integrity behavior of 18650 lithium-ion batteries, Sci. Rep-UK. 6 (2016).
[24] J. Zhang, D. Ding, X. Xu, Y. Gao, G. Chen, W. Chen, et al., Effect of Ce addition on the mechanical and electrochemical properties of a lithium battery shell alloy, J. Alloys Compd. 617 (2014) 665–669.
[25] J. Du, D. Ding, Z. Xu, J. Zhang, W. Zhang, Y. Gao, et al., Effect of CeLa addition on the microstructures and mechanical properties of Al-Cu-Mn-Mg-Fe alloy, Mater. Charact. 123 (2017) 42–50.
[26] X. Zhang, T. Wierzbicki, Characterization of plasticity and fracture of shell casing of lithium-ion cylindrical battery, J. Power Sources 280 (2015) 47–56.
[27] J. Xu, B. Liu, X. Wang, D. Hu, Computational model of 18650 lithium-ion battery with coupled strain rate and SOC dependencies, Appl. Energy 172 (2016) 180–189.
[28] J. Luo, C.Y. Dai, Z. Wang, K. Liu, W.G. Mao, D.N. Fang, et al., In-situ measurements of mechanical and volume change of LiCoO2 lithium-ion batteries during repeated charge–discharge cycling by using digital image correlation, Measurement 94 (2016) 759–770.
[29] M.A. Iqbal, K. Senthil, P. Sharma, N.K. Gupta, An investigation of the constitutive behavior of Armox 500T steel and armor piercing incendiary projectile material, Int. J. Impact Eng. 96 (2016) 146–164.
[30] J. Dean, C.S. Dunleavy, P.M. Brown, T.W. Clyne, Energy absorption during projectile perforation of thin steel plates and the kinetic energy of ejected fragments, Int. J. Impact Eng. 36 (2009) 1250–1258.
[31] Y.K. Xiao, H. Wu, Q. Fang, W. Zhang, X.Z. Kong, Hemispherical nosed steel projectile high-speed penetration into aluminum target, Mater. Des. 133 (2017) 237–254.
[32] D.Y. Hu, K.P. Meng, H.L. Jiang, J. Xu, R.R. Liu, Strain rate dependent constitutive behavior investigation of AerMet 100 steel, Mater. Des. 87 (2015) 759–772.
[33] J.W. Hancock, A.C. Mackenzie, On the mechanisms of ductile failure in high-strength steels subjected to multi-axial stress-states, J. Mech. Phys. Solids 24 (1976) 147–160.
[34] S.R. Guillow, G. Lu, R.H. Grzebieta, Quasi-static axial compression of thin-walled circular aluminium tubes, Int. J. Mech. Sci. 43 (2001) 2103–2123.
[35] A.A. Singace, H. Elsobky, T.Y. Reddy, On the eccentricity factor in the progressive crushing of tubes, Int. J. Solids Struct. 32 (1995) 3589–3602.
[36] M.A. Iqbal, K. Senthil, P. Bhargava, N.K. Gupta, The characterization and ballistic evaluation of mild steel, Int. J. Impact Eng. 78 (2015) 98–113.
[37] K. Senthil, M.A. Iqbal, P.S. Chandel, N.K. Gupta, Study of the constitutive behavior of 7075-T651 aluminum alloy, Int. J. Impact Eng. 108 (2017) 171–190.
[38] J. Xu, B. Liu, L. Wang, S. Shang, Dynamic mechanical integrity of cylindrical lithium-ion battery cell upon crushing, Eng. Fail. Anal. 53 (2015) 97–110.